International Information and Engineering Technology Association
Advancing the World of Information and Engineering

Traitement du Signal
Vol. 41, No. 2, April, 2024, pp. 653-668
Journal homepage: http://iieta.org/journals/ts

Ultrasonic Synthetic Aperture Imaging for Inner Defect of Concrete Based on Delay-Multiple-and-Sum

Lifan Rong[1,2*], Yiqiong Chen[3], Jinlin Hu[2], Yunlong Liu[2], Haoran Li[1]

[1] School of Safety Engineering and Emergency Management, Shijiazhuang Tiedao University, Shijiazhuang 050043, China
[2] Collaborative Innovation Center for Performance and Security of Large-scale Infrastructure, Shijiazhuang Tiedao University, Shijiazhuang 050043, China
[3] School of Transportation, Shijiazhuang Tiedao University, Shijiazhuang 050043, China

Corresponding Author Email: lfrong@stdu.edu.cn

https://doi.org/10.18280/ts.410209

Received: 2 January 2024
Revised: 9 March 2024
Accepted: 26 March 2024
Available online: 30 April 2024

Keywords:
ultrasonic tests, concrete inner defect, SAFT, DMAS, imaging quality

ABSTRACT

Ultrasonic imaging is a promising NDT method to precisely detect the inner defects inside concrete, which is benefit to the maintenance decision and safety assurance of concrete structure engineering. In order to effectively improve the imaging quality, a DMAS algorithm is introduced to replace DAS beamformer in SAFT method to suppress the strong structure noise of concrete and improve the imaging resolution, meanwhile amplitude compensation algorithm is used to preprocess the collected signals to improve the image contrast of the defects located in deep depth. Several numerical models and real concrete structures contain void defects with different size and locations were prepared, and ultrasonic tests were conducted by using ultrasonic array. Both the numerical simulation and real tests on concrete structures can verify the performance of the proposed method. Compared with the traditional SAFT method, the proposed method DMAS-SAFT can reconstructs higher quality images, which have significant improvement in signal-to-noise (SNR) and lateral resolution, while consumes almost the same computational time.

1. INTRODUCTION

Concrete is one of the materials widely used in civil construction, such as buildings, bridges, tunnels and so on. The quality of concrete is extremely important for structure safety and durability. However, due to the unstrict construction process control in some time, aging, long term loading and environment factors, some inner defects appear and may continue to expand. The inner defects including cracks, voids and honeycomb can weaken the concrete durability, reduce the bearing capacity of structures, or even lead to structural failure. Therefore, the accurate detection for inner defects is crucial to ensure concrete structures safety and reliability [1, 2].

The internal defects existing in concrete cannot be directly visible, so destructive method, such as core drilling, is usually adopted to evaluate the internal condition of concrete. Compared with the traditional destructive method, the nondestructive test (NDT) methods with penetrating capabilities are effective and have been widely used for inner defect detection in civil structures [3]. The common NDT methods are infrared thermography [4], ground-penetrating radar [5], X-ray [6], impact echo [7], and ultrasonic testing [8]. Among of those methods, ultrasonic testing has unique advantages, for example, high ultrasonic energy, strong penetration and good directivity, and is effective and reliable in detecting the internal quality of structure based on the ultrasound propagating inside concrete [9].

Ultrasonic synthetic aperture focusing technology (SAFT) is one of the rapidly developed ultrasonic test methods used in concrete internal defects. During the test, a pair of ultrasonic transducers is adopted to emit ultrasound into concrete and receive the echo signals along measure line, then several signals collected are processed by using delay and sum (DAS) to obtain visual image for the interior section below measure line, And the inner defects can be easily identified and located from the section image [10-12]. Additionally, only one measure surface is needed in SAFT method, which is suitable for the most concrete structures. Hence, it seems to be the most promising method to detect concrete internal defects.

The imaging quality is the key to detect defects inside concrete. However, due to the strong heterogeneity, the imaging quality for concrete is still worse than homogeneous materials, which also has significant effect on the detection precision of concrete internal defects. The Concrete is a composite material composed of aggregates bonded together with cement, while reinforced concrete (RC) consists of concrete and steel bars, which means numerous material interfaces exist in concrete or RC. When ultrasonic wave propagates across the material interfaces, refraction and reflection occur. So when ultrasonic wave propagates in the concrete or RC, multiple refraction and reflection occur on the numerous material interfaces and results in strong structure noise and high attenuation of ultrasonic wave, both of which seriously affect the image resolution.

In recent years, lots of researchers have devoted to enhance the image quality of concrete interior section in order to increase the detection precision. An ultrasonic array was used to increase the number of the collected signals, and corresponding array-based synthetic aperture focusing imaging algorithm was proposed to improve the image quality [13]. Considered the effect of concrete heterogeneity on measured velocity, Lin proposed a new wave velocity calculating method based on dispersion analysis, and the more accurate velocity improves the ultrasonic wave focusing performance and thus increases the image quality [14]. Variational mode decomposition algorithm is introduced to pre-process signals to improve the signal SNR before signal focus imaging, and bilateral filtering is adopted to process the image edge to improve the SAFT image quality [15].

Based on DAS algorithm, total focus method (TFM) is developed from SAFT, which uses full matrix capture mode to further increase the number of collected signals in order to improve ultrasonic imaging quality [16, 17]. Based on TFM, time reversal (TR) [18, 19] and phase coherence imaging (PCI) [20] are used to reduce the influence of the serious and complicated scattering ultrasound on the imaging, and obtain ultrasonic images with high resolution [21]. However, due to the large amount of data acquisition and processing problems, the image reconstruction with high resolution usually requires high computational cost by TFM, which limited TFM practical field application for detecting concrete inner defects [22].

The ultrasonic imaging method reconstructing image with high resolution while consuming short computational time is always expected for the detection of inner defects within concrete. Compared with DAS, an alternative non-linear beamforming algorithm with better performance in noise suppression called Delay-multiply-and-sum (DMAS) is proposed to enhance the image quality with higher contrast and narrower main lobe [23, 24]. The application of DMAS in photoacoustic has been proved that it can significant improve the ultrasonic B-mode image quality [25, 26]. By considering coherence factor, the quality of reconstructed images based on DMAS can be further improved [27]. Teng [28] had modified DMAS with synthetic focusing to optimize TFM for obtaining high resolution images. Therefore, DMAS algorithm seems to have great potential to replace DAS in SAFT method to further improve the ultrasonic imaging performance for detection inner defects within concrete.

In this study, in order to reduce the adverse effect of strong structure noise of concrete on ultrasonic imaging quality, DMAS algorithm is introduced to replace DAS beamformer in SAFT, meanwhile amplitude compensation algorithm is used to preprocess the collected signals to improve the amplitude of signals reflected by defects located in deep depth. Several ultrasonic tests for reinforced concrete containing internal defects with different size and location were conducted, and the images reconstructed by SATF and DMAS-SAFT were compared to verify the imaging performance of DMAS-SAFT for concrete inner defects.

2. METHOD

2.1 SAFT method

Original SAFT technology using for detection of inner defects in concrete is that a pair of ultrasound transducers moves along the measure line, one of them emit ultrasound into concrete, while the other one receives the signal reflected from concrete interior structure. According to the coordinate of each imaging point, the received signals is delayed appropriately and then synthesized to focusing point by point based on DAS. Recently, ultrasonic array is widely used to increase the testing speed and received signals number to enhance the imaging quality, as follow:

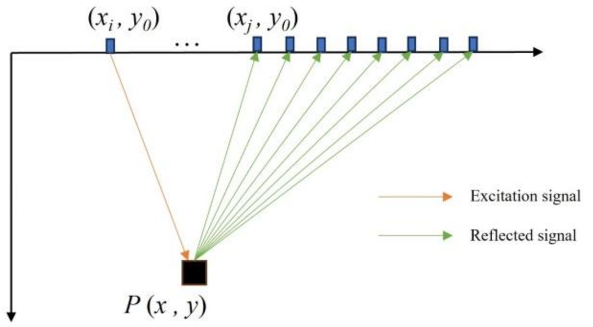

Figure 1. Ultrasonic array and signals excitation-receiving mode

As shown in Figure 1, an ultrasonic array consists of N transducers, when one transducer excites and transmits ultrasound into concrete, the other transducers behind the transmitting transducer receive the signals. Assume the ultrasonic wave speed in the test area is v, the i-th transducer is transmitting transducer with coordinates (x_i, y_0), the j-th transducer is receiving transducer with coordinates (x_j, y_0), and the coordinate of reflecting point P is (x, z). The signal exiting by the i-th transducer and receiving by the j-th transducer is denoted as signal$_{ij}(t)$. The delay time τ_P experienced by the ultrasound is transmitted from the position of transducer i and reflected back to transducer j after via reflecting point P, is calculated as:

$$\tau_P = \frac{(x-x_i)^2+(y-y_0)^2}{v} + \frac{(x-x_j)^2+(y-y_0)^2}{v} \tag{1}$$

Due to the delay time, the corresponding value of reflecting point $P(x, y)$ in signal$_{ij}(t)$ can be expressed as:

$$I_{\mathrm{ij}}(P) = signal_{ij}(\tau_P) \tag{2}$$

And the imaging value of point P can be obtained by Eq. (3):

$$y_{-SAFT}(P) = \sum_{i=1}^{N-1} \sum_{j=i+1}^{N} signal_{ij}(\tau_p) \tag{3}$$

In order to suppress side lobes, an apodization factor k is introduced to imaging process, and Eq. (3) is expressed as:

$$y_{-SAFT}(P) = \sum_{i=1}^{N-1} \sum_{j=i+1}^{N} k_{\mathrm{ij}}(x,y) signal_{ij}(\tau_p) \tag{4}$$

The apodization function is described as follow:

$$\begin{aligned} k_{ij}(x,y) &= (\cos\alpha \times \cos\beta)^w \\ &= \left(\frac{y}{\sqrt{(x-x_i)^2+y^2}} \times \frac{y}{\sqrt{(x-x_j)^2+y^2}} \right)^w \end{aligned} \tag{5}$$

where, α is the included angle between the emission line from the transmitting point to the imaging point and the normal line, while β is the reflection line form the receiving point to the imaging point and the normal line. The power of number ω is accommodation coefficient to adjust the receiving aperture size in different depth, ω=1 for generally imaging and ω can be greater than 1 for imaging in deep depth.

2.2 DMAS-SAFT method

DMAS is a novel nonlinear beamforming algorithm which introduces spatial coherence in signals received by different transducers into DAS beamforming process by adding cross-multiplication of signals before summing. The operation of cross-multiplication between signals can be interpreted as the aperture spatial auto-correlation, which means the spatial correlation among all the receiving signals is computed. By additionally considering the spatial coherence in signals, the adverse effect of the incoherence signals is suppressed, thus the DMAS beamforming results are certainly more accurate than DAS beamforming results. The DMAS output is obtained as:

$$y_{DMAS}(t)=\sum_{i=1}^{N}\sum_{j=i+1}^{N}S_i(t)S_j(t) \tag{6}$$

where, $S_i(t)$ is the time-domain receiving signal, N is the number of receiving signals. The cross–multiplication of signals is equivalent to take the spatial correlation among all receiving signals in to account, and also effectively increases the data volume of the signals. Hence, DMAS can provide clearer image with higher resolution and back contrast than DAS.

In this study, a modified SAFT method is proposed and termed as DMAS-SAF., In the method, DMAS beamforming algorithm is integrated into SAFT by replacing DAS algorithm to improve the imaging quality of concrete. Considering both the transmitter and receiver in the ultrasonic array for cross-correlation of calculation, for imaging point $P(x, y)$, the focused signal of DMAS-SAFT is expressed as:

$$y_{DMAS-SAFT}(P)=\sum_{i=2}^{N}\sum_{j=i+1}^{N}S_i(P)S_j(P) \tag{7}$$

where, $S_i(P)$ is the DMAS processing result of all signals received by the i-th transducer, it can be calculated as:

$$\begin{aligned}&S_i(P)\\&=\sum_{m=1}^{N-1}\sum_{n=m+1}^{N-1}k_{mi}(x,y)signal_{(m,i)}(\tau_P)k_{ni}(x,y)signal_{(n,i)}(\tau_P)\end{aligned} \tag{8}$$

where, τ_{p} is calculated by Eq. (1). By the cross-multiplication, the sample size is significantly increased, which can effectively contribute for noise suppression. But the operation of cross-multiplication for all of the signals received by ultrasonic array is computational expensive, which leads that the computational efficiency is too low to meet the requirement of quick imaging for concrete in situ.

In order to reduce the computational load, the spatial information of the received array signals is considered, while the spatial information of transmission array in signals is ignored. Thus, $S_i(P)$ can be simplified as the DAS processing result of all signals received by the i-th transducer which transmitted by different transmitters, it can be expressed as:

$$S_i(P)=\sum_{m=1}^{N-1}k_{mi}(x,y)signal_{(m,i)}(\tau_P) \tag{9}$$

Subsequently, the focused result of DMAS-SAFT at imaging point P is still calculated by Eq. (7). The focused results at all the other imaging points can be obtained by repeating above processing, and to reconstruct the section image of concrete interior structure below ultrasonic array.

After calculating all imaging points, the focusing results of all imaging points are formed into a matrix ***Amp***. This is due to a mathematical fact that by multiplying the RF signals, have almost similar frequency content (e.g. band centered at f_0), two new components are generated in the amplitude spectrum. Output signals, that is, one centered at f_0-f_0=0 and one centered at f_0+f_0=2f_0. The spectrum diagram of ***Amp*** is mainly composed of direct current (DC) components and second harmonics. The second harmonic has high frequency and short wavelength. This will lead to improvements in imaging resolution. In order to retain the second harmonic to reconstruct the image, a filter with a center frequency of 2f_0 is applied to the image data matrix ***Amp***, and the cutoff frequency of the filter is determined according to the spectrogram to retain the entire second harmonic and filter out the DC component and clutter.

2.3 C-DMAS-SAFT method

When inspecting concrete at large depths, ultrasonic waves are severely attenuated and the reflected signals are very weak, resulting in poor imaging results. In order to detect the deep layers of the structure, we increased the apodization coefficient ω to the power of 3, which reduced the aperture in the shallow layer and increased the aperture in the deep layer. Based on the basic law of exponential attenuation of ultrasonic waves in concrete, we performed amplitude compensation to enhance large depth Defect reflection intensity in the case of concrete.

An important reason for the poor performance of ultrasonic imaging is that there is a huge difference in amplitude between the collected surface direct wave signal and the bottom echo signal, which directly leads to the reflection signal deep in the concrete being submerged. In order to reduce the difference between the direct wave and the bottom echo and improve the quality of concrete ultrasonic imaging, the relative attenuation coefficient is used to characterize the attenuation degree of each reflected echo inside the concrete relative to the surface direct wave. The relative attenuation coefficient α is calculated as:

$$\alpha=-\frac{20}{x}\log(\frac{A_x}{A_d}) \tag{10}$$

where, A_d is the peak value of the direct wave, A_x is the peak value of the bottom reflected wave, x is the propagation distance of ultrasonic waves. The relative attenuation coefficient represents the attenuation degree of each reflected echo inside the concrete relative to the direct wave on the surface.

The relative attenuation coefficient α is calculated from the data transmitted and received by adjacent array elements, and the average value of these N-1 attenuation coefficients is used as the relative attenuation coefficient. The calculated relative attenuation curve is $\frac{A_x}{A_d} = 10^{-\frac{\alpha \cdot x}{20}}$, take the reciprocal of it to get $10^{\alpha \cdot \frac{x}{20}}$, this is the relative compensation curve corresponding to each propagation distance in the ultrasonic echo signal (Figure 2).

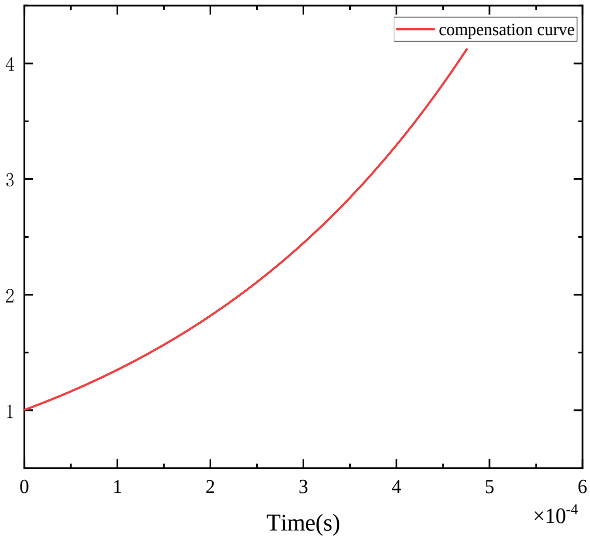

Figure 2. The relative compensation coefficient curve

By multiplying each point in the original ultrasonic echo signal by the corresponding compensation coefficient, the amplitude compensated ultrasonic echo signal can be obtained. Perform amplitude compensation preprocessing on the original signal, and increase the power of the apodization factor to 3 to perform DMAS-SAFT imaging. The method is named compensation-based DMAS-SAFT imaging method (C-DMAS-SAFT).

3. SIMULATION METHOD AND RESULT

This part mainly describes the experimental settings of the simulation and the analysis of the simulation results, and comparatively studies the improvement effect of the improved method on the imaging quality.

3.1 Simulation setup

In order to validate the effectiveness of the proposed DMAS-SAFT imaging method, two sets of reinforced concrete structures with void defects were simulated, with the defects located at shallow and deep locations of the structures to evaluate the image spatial resolution and noise suppression capability, as well as the deep defect detection capability. Three-dimensional fine-scale numerical models of these groups of reinforced concrete were simulated and ultrasonic echo signals were acquired using Abaqus software. In addition, both pre-processing and post-processing imaging of the signals were run in MATLAB.

In this study, six finite element models were set up, where the defects were located in the shallow layer and the deep layer. The size of the defects was set to 60mm, 50mm, and 40mm in length respectively. In the first set of simulations, a layer of steel bars was set up. The diameter of the steel bars used in this simulation study was 25 mm. The defect was located below the middle of the steel bar with a thickness of 30 mm. The upper surface of the defect was 260 mm away from the detection surface. In the second group of simulations, two layers of steel bars were arranged. The defect was located in the middle of the second layer of steel bars. The thickness was also 30 mm. The upper surface of the defect was 370 mm away from the detection surface. These defects were designed as rectangular structures to facilitate defect location and evaluation of detection capabilities. The specific model size settings are shown in Figure 3.

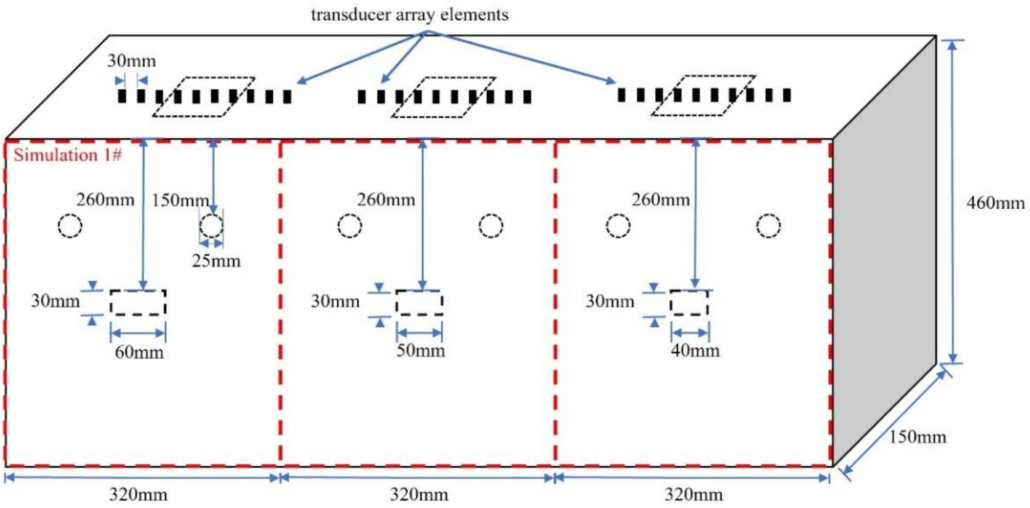

(a) The defects are located in a shallow position

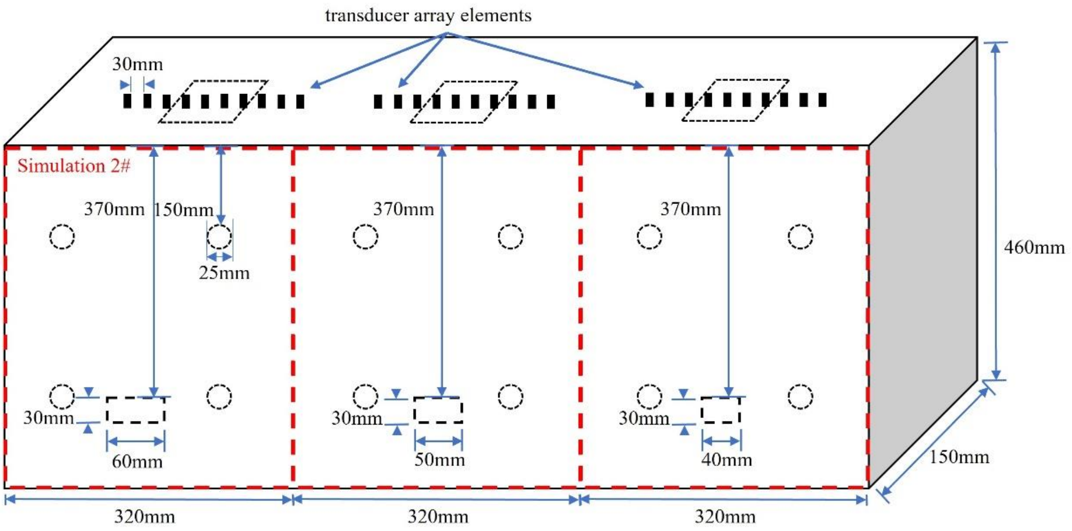

(b) The defects are located in a deep position

Figure 3. Schematic diagram of the dimensions and sensor arrangement of the finite element model

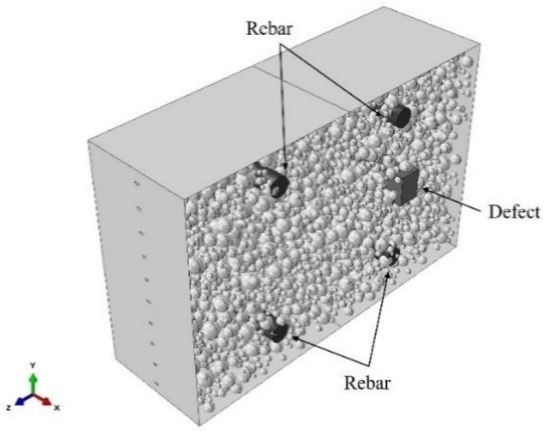

Figure 4. Schematic diagram of the three-dimensional mesoscopic numerical model. This model example shows an inner defect with a length of 40mm and located at a deep position

Table 1. Numerical model structural material parameters

Material	Modulus of Material (MPa)	Poisson's	Density (kg·m^{-3})
Coarse aggregate	5.5×10^4	0.47	2.9×10^3
Cement mortar	1.92×10^4	0.35	1.9×10^3
Rebar	2.06×105	0.28	7.85×103
Defect	1	0.45	1.4×103

The concrete mesoscopic model was generated through the random placement method of aggregates, and the steel bars were laid out in the concrete model with reference to the tunnel lining reinforcement pattern. The material parameters of the model are shown in Table 1.

The simulation model size is 320 mm×150 mm×460 mm, and the grid size is 0.5 mm. Infinite elements were set up around the concrete numerical model to eliminate boundary echo interference. Ten excitation and receiving signal area were arranged on the top of the model to simulate sensors. The sensors were 30mm apart. The Hanning window modulation signal with a main frequency of 50KHz was used as the excitation signal, and was loaded into the model in the form of horizontal shear pulses to generate horizontal shear waves (SH waves). The schematic diagram of the finite element model established by ABAQUS is shown in Figure 4.

3.2 Signal reception and processing

The ultrasonic echo signals were collected according to the synthetic aperture transmitting and receiving method. It was excited by one array element, and all the remaining array elements that had not yet been excited were received. The schematic diagram of the ultrasonic echo signals is shown in Figure 5.

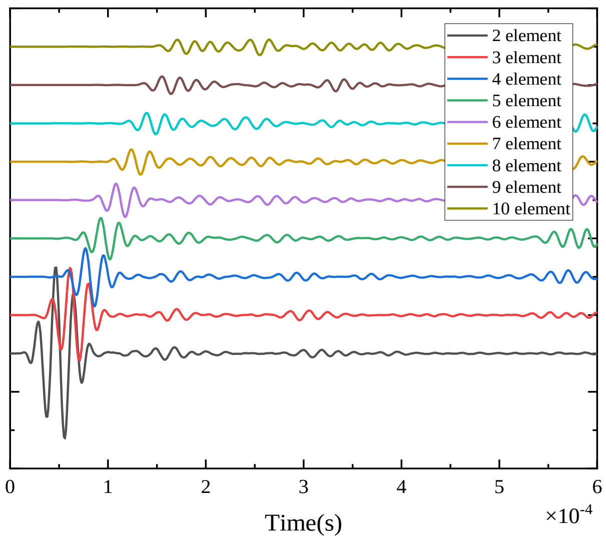

Figure 5. Schematic diagram of ultrasonic echo signals. This is the echo signal transmitted by the first array element and received by all other arrays

For defects in deep locations, the echo signals were compensated based on the calculated ultrasonic attenuation coefficient. The compensated signals can better feedback the reflection echoes in the deep structure and improve the imaging accuracy of the deep structure. It was clear that the compensated signals increased the deep defect echo compared to the uncompensated signal (Figure 6). In addition, the noise in the echo signal also increased. The effectiveness of the DMAS-SAFT method was verified through simulation studies of shallow internal defects of different sizes. For deep-located defects, we increased the power of the apodization factor to obtain larger apertures while compensating for signal attenuation. The effectiveness of the C-DMAS-SAFT imaging method was demonstrated through the detection of defects deep within reinforced concrete structures.

3.3 Imaging results and analysis

In the first simulation, the image data amplitude ***Amp*** after delayed accumulation and multiplication was subjected to two-dimensional Fourier transform for frequency domain analysis. From the spectrogram, we can see two frequency components, namely a DC component centered on zero, and a second harmonic centered on twice the center frequency $2f_0$, consisting of two different phases. The image data were filtered by applying a bandpass filter, retaining the second harmonic signal for image reconstruction. The bandwidth of the bandpass filter was set according to the image spectrogram to ensure that the second harmonic was fully included (Figure 7).

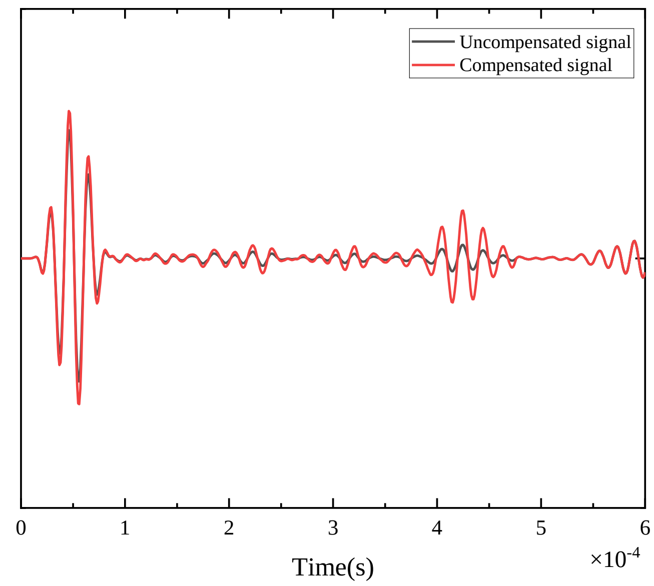

Figure 6. Comparison of compensated and uncompensated echo signals. This original echo signal was received by the fifth element and transmitted by the first element

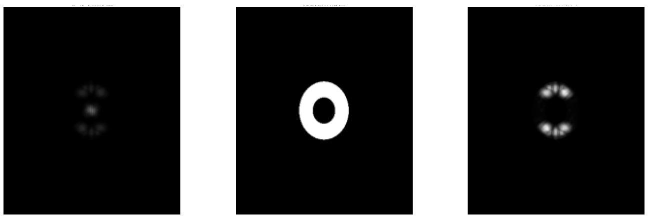

Figure 7. Schematic diagram of spectrum analysis. (a) Represents the spectrum of the image data before filtering, (b) The spectrum of the filter, and (c) The spectrum of the image data after filtering

In the results of the first simulation, both SAFT and DMAS-SAFT imaging methods can show the correct location of defects and rebars. However, it is obvious that the imaging results of SAFT were affected by considerable background noise. In the case of different defect sizes, it is observed that as the defect size decreases, the detection ability of SAFT decreases, resulting in poor detection results for 40mm defects, in which the defect energy is significantly reduced and there are obvious artifacts (Figure 8a). In contrast, in DMAS-SAFT imaging, interference from background noise was effectively suppressed, eliminating artifacts and enabling precise localization of defects and rebars. This led to a significant enhancement in image quality (Figure 8b). DMAS-SAFT can effectively reduce the noise present in the image, resulting in clearer images that make it easier to distinguish between true defect features and artifacts caused by noise, thereby enhancing the ability to accurately locate and characterize defects. On the other hand, there is also an improvement in resolution, contrast, and the ability to resolve features in the image that are closely positioned or of small size.

In order to further analyze the imaging performance of the DMAS-SAFT method in detail, a comparative analysis of the transverse projection profiles obtained by the SAFT and DMAS-SAFT methods was performed. The analysis was centered on the middle row of data representing defect thickness. As shown in Figure 9, the clutter amplitude was significantly reduced to almost non-existence compared to the SAFT projection at the lateral end of the DMAS-SAFT projection curve. This comparison vividly demonstrated the superior noise suppression capabilities of the DMAS-SAFT method. Furthermore, the lateral projection width of the DMAS-SAFT image more accurately approximates the actual defect length, as opposed to the wider projection generated by SAFT. This improved accuracy is quantified in Table 2, which lists the lateral projected width error at -20dB. The error is significantly smaller compared to DMAS-SAFT projection, indicating more precise imaging capabilities. This enhancement is particularly evident in lateral resolution, which is critical for accurate localization and characterization of defects. Therefore, DMAS-SAFT can provide higher resolution and more accurate representation of detected defects.

The results of the second simulation exhibited the defects set at deep location. In the results of the traditional SAFT imaging method, the acoustic image energy at the position of the first layer of rebar was strong, while the energy at the second layer of rebar was slightly weaker. The energy at the position of the void defects was smaller, making it disadvantageous to identify defects through ultrasound imaging results. (Figure 10a). The imaging results with the improved DMAS-SAFT method were of higher quality than those of the traditional SAFT method. The structural noise in the imaging results was further suppressed and the imaging resolution was improved. The acoustic image energy was evenly distributed at the first layer of steel bars, and the noise was greatly suppressed. Additionally, the acoustic image energy at the second layer of rebars was increased. More importantly, the acoustic image energy at the location of void defects was significantly enhanced (Figure 10b). In DMAS-SAFT imaging, the defect detection was already effective. However, to further identify the characteristics of deep defects, we had increased the dynamic amplitude apodization adjustment coefficient. This coefficient significantly influenced the acoustic image energy at the locations of voids and rebars. In addition, we compensated for the signal attenuation of the echo signal inside the structure, significantly enhancing the acoustic energy of reflectors such as voids and steel bars at deep location. This was advantageous for identifying deep void defects. However, the acoustic energy of the shallow first layer of steel bars may decrease slightly in the results (Figure 10c).

In the second set of simulations, a comparative analysis of the lateral resolution of imaging using different imaging methods—DMAS-SAFT, C-DMAS-SAFT, and SAFT—was performed. The DMAS-SAFT and C-DMAS-SAFT curves exhibited very low amplitudes at locations without rebars and defects, nearly approaching zero. This demonstrated the superior noise suppression capabilities of these methods over traditional SAFT. In terms of defect detection, the waveform widths at the defect locations for DMAS-SAFT and C-DMAS-SAFT were noticeably closer to the actual size of the defects compared to those obtained by SAFT. Moreover, the lower amplitude between adjacent peaks allowed for the clear distinction of two separate targets, namely defects and rebars. Particularly with C-DMAS-SAFT, the highest amplitude was observed at the locations of defects, significantly enhancing the energy and thus making the characteristics of the defects more distinct. This was especially evident in the detection of 40mm defects, where the amplitude compensation led to a notable increase in defect energy, clearly demonstrating the C-DMAS-SAFT method's effectiveness. (Figure 11). The comparison of the errors between the actual defect sizes and the widths of their projections at the -20dB level using different imaging methods was presented in Table 3. This comparison allowed for an assessment of the accuracy of each method in approximating the true dimensions of the defects.

Table 2. Error between the preset defect length and the lateral projected defect width at -20 dB for images imaged in the simulation using conventional SAFT, DMAS- SAFT methods

Width	Depth	SAFT	DMAS-SAFT
60mm	260mm	101.64	13.75
50mm	260mm	67.36	27.22
40mm	260mm	65.92	30.48

Table 3. Error between the preset defect length and the lateral projected defect width at -20 dB for images imaged in the simulation using conventional SAFT, DMAS- SAFT and C-DMAS-SAFT methods (unit: mm)

Width	Depth	SAFT	DMAS-SAFT	C-DMAS-SAFT
60 mm	370 mm	67.38	14.37	14.21
50 mm	370 mm	103.22	21.26	17.89
40 mm	370 mm	66.84	32.55	33.33

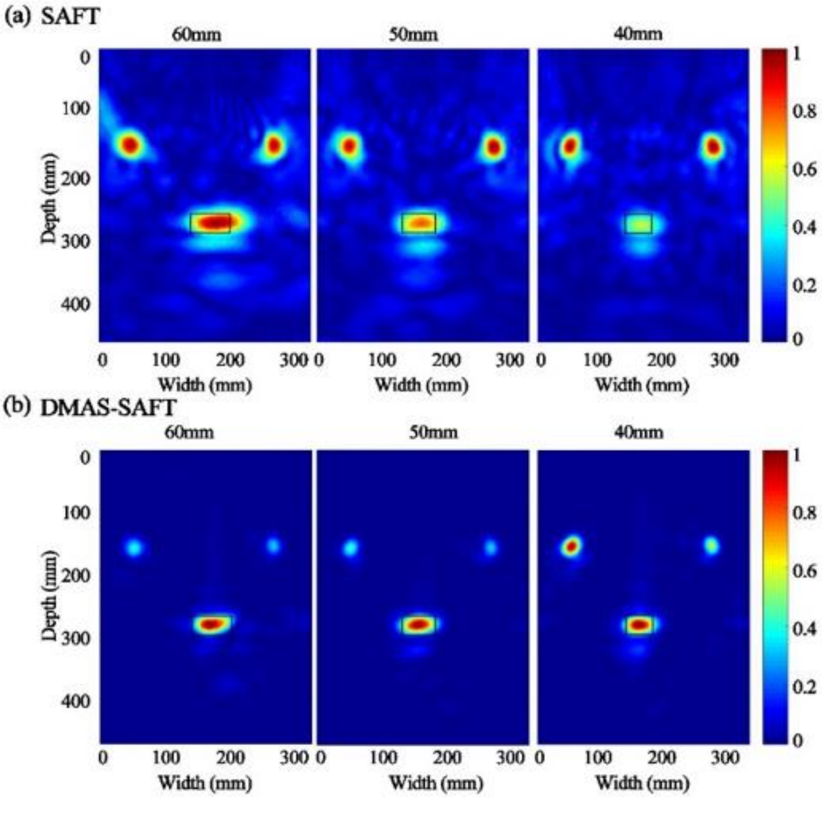

Figure 8. Imaging results of the first simulation. (a) Displays the imaging result using the SAFT method for defects of different sizes. (b) The imaging result using the DMAS-SAFT method with m=1

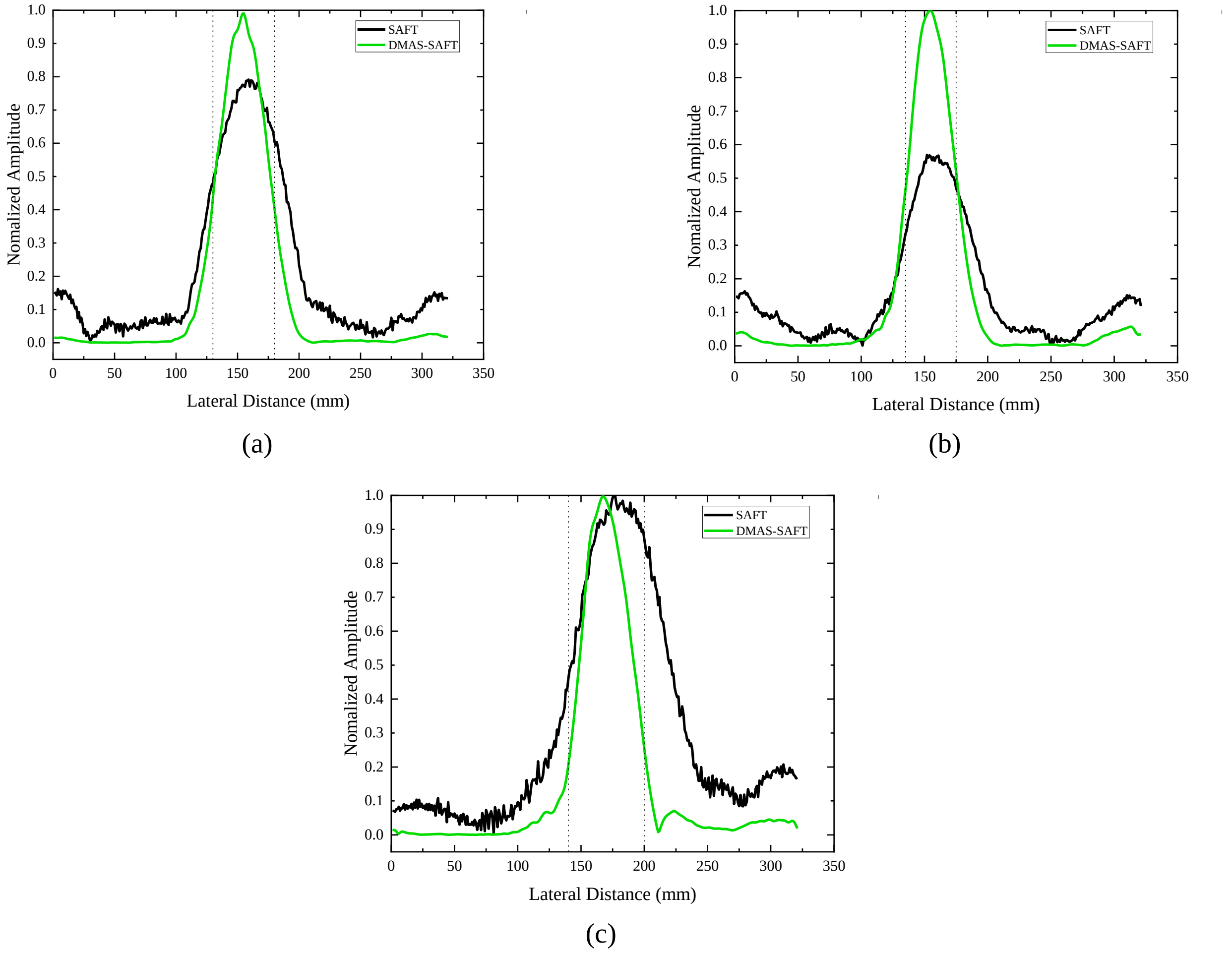

(a)

(b)

(c)

Figure 9. Comparison of lateral projection using SAFT, DMAS-SAFT for defects of various lengths; (a) 60 mm, (b) 50 mm, (c) 40 mm in shallow positions. The dotted lines represent the actual abscissa position where the defect. (unit: mm)

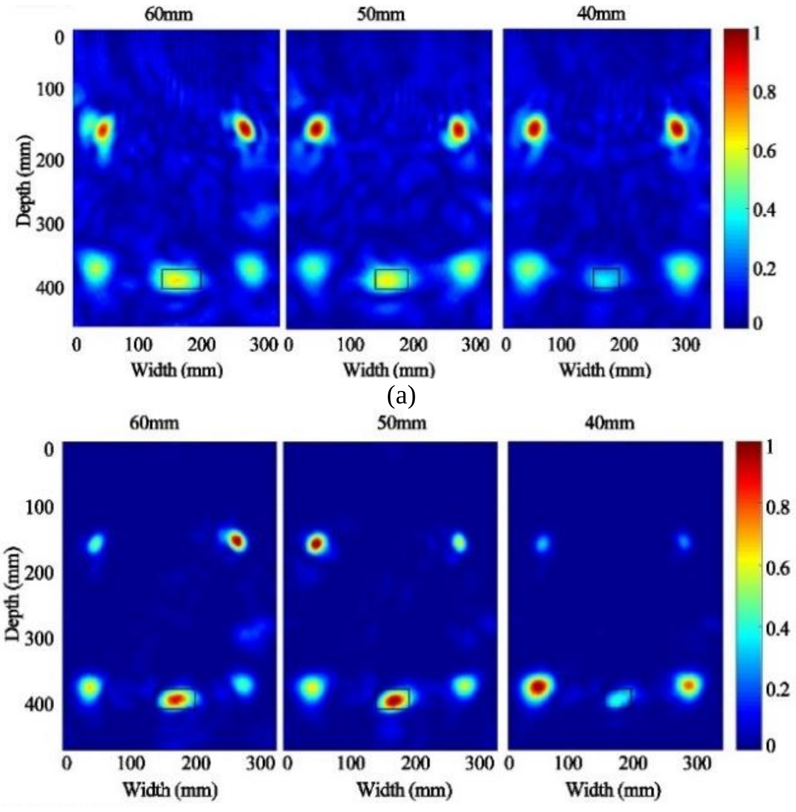

(a)

(b)

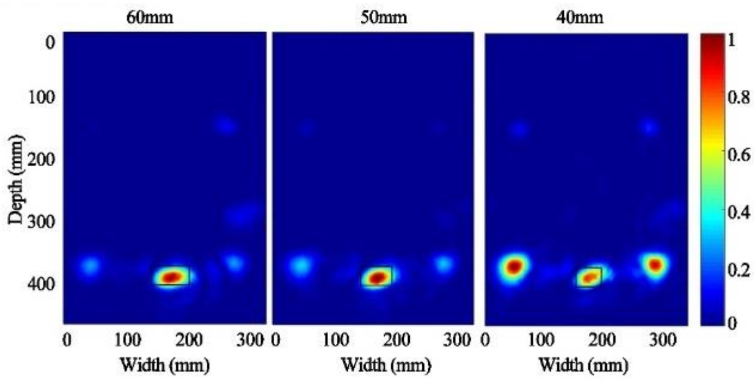

(c)

Figure 10. Imaging results of the second simulation. (a) Displays the imaging result using the SAFT method for defects of different sizes. (b) The imaging result using the DMAS-SAFT method. (c) The imaging result using the C-DMAS-SAFT method

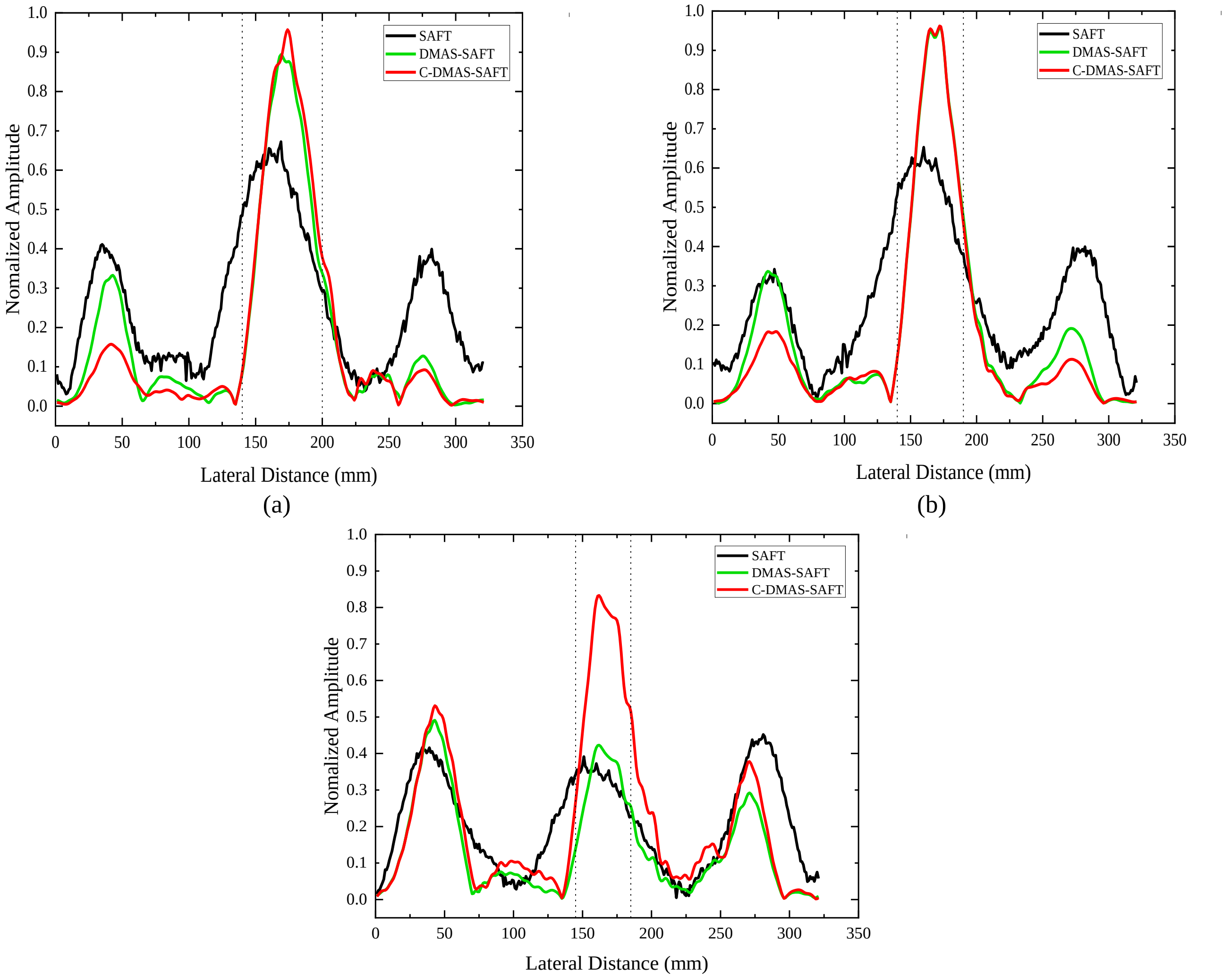

(a)

(b)

(c)

Figure 11. The comparison of lateral projections in the second simulation for defects at depth location. (a) corresponds to the 60mm defect, (b) to the 50mm defect, and (c) to the 40mm defect. The dotted lines across the graphs indicate the actual positions corresponding to the defects

To quantify the noise suppression ability of DMAS-SAFT method and C-DMAS-SAFT method, the signal-to-noise ratio (SNR) was calculated as:

$$SNR_{dB} = 20\log_{10}\frac{mean(I_{defect})}{mean(I_{noise})} \tag{11}$$

where, $mean(I_{defect})$ represents the average amplitude at the preset defect position and $mean(I_{noise})$ is the average amplitude of the background noise without defect and rebars. The amplitude of the signal from the rebar's position is not included in the SNR calculation. The presence of the rebars does not adversely affect the imaging quality of the measurements being made. Moreover, the main focus of the imaging is not the rebars, but the defects within the reinforced concrete structure. By excluding the signal amplitude of the steel bars from the signal and noise components of the SNR calculation, and mainly focusing on the defects and background noise, this ensures that the SNR calculation more accurately reflects the imaging quality of the defects.

In the first simulation, the efficacy of DMAS-SAFT was assessed by comparing its SNR improvements over the conventional SAFT method. The details were illustrated in Table 4. For the 60 mm defect, the SNR achieved using DMAS-SAFT was 27.90 dB, which represents an increase of 12.84 dB over the standard SAFT. Similarly, for the 50mm defect, the DMAS-SAFT achieved an SNR of 32.31 dB, outperforming the traditional method by 15.84 dB. Most notably, with the 40mm defect, the DMAS-SAFT reached an SNR of 33.06 dB, surpassing the conventional SAFT by 16.27 dB. These results clearly indicate a significant enhancement in SNR with the DMAS-SAFT method, especially in detecting smaller defects. The improvement rates were approximately 85.26% for the 60mm defect, 96.17% for the 50 mm defect, and 96.90% for the 40 mm defect. The SNR of DMAS-SAFT is on average 92.78% higher than that of traditional SAFT, further demonstrating the advanced capabilities of DMAS-SAFT in noise suppression.

In the second simulation the defect was set in a deep position. Through increasing the power of the apodization factor and performing amplitude compensation on the echo signal, the energy at the defect's location was enhanced, while the noise level in the deep layers was also increased. The noise suppression abilities of DMAS-SAFT and C-DMAS-SAFT were quantitatively evaluated and contrasted with traditional SAFT.

In the second simulation, the SNR results are detailed in Table 5. For a defect size of 60mm, the SNR for DMAS-SAFT was measured at 25.3 dB, which is an increase of 12.56 dB over traditional SAFT. The C-DMAS-SAFT method further enhanced this performance, achieving an SNR of 27.74 dB, which is a 196.23% increase over traditional SAFT. For the 50mm defect, the SNR of DMAS-SAFT saw an 11.71 dB increase compared to SAFT, with C-DMAS-SAFT reaching 31.36 dB, an increase of 111.89%. In the case of the smallest measured defect at 40mm, DMAS-SAFT reported an SNR of 23.77 dB, which is 11.67 dB higher than SAFT, while C-DMAS-SAFT reached 26.81 dB, marking an increase of 121.57%. The average increase rate for the SNR across the different defect sizes using the C-DMAS-SAFT method compared to traditional SAFT is approximately 143.23%.

Table 4. The signal-to-noise ratio (SNR) of the imaging results in the first simulation

Width	Depth	SAFT	DMAS-SAFT
60 mm	260 mm	15.06 dB	27.90 dB
50 mm	260 mm	16.47 dB	32.31 dB
40 mm	260 mm	16.79 dB	33.06 dB

Table 5. The SNR of the imaging results in the second simulation

Width	Depth	SAFT	DMAS-SAFT	C-DMAS-SAFT
60 mm	370 mm	12.74 dB	25.30 dB	27.74 dB
50 mm	370 mm	14.80 dB	26.51 dB	31.36 dB
40 mm	370 mm	12.10 dB	23.77 dB	26.81 dB

3.4 Discuss on computational performance for modified methods

In practice, for data from an ultrasound array with 10 elements, the time cost of using the SAFT method was 1.559 seconds. The time cost of using the DMAS-SAFT method was 1.639 seconds, while the time cost of using the C-DMAS-SAFT method was 1.78 seconds. Time was measured on a personal computer equipped with a Core i5 1.70 GHz CPU and 16 GB RAM. The results confirmed that the DMAS-SAFT method and C-DMAS-SAFT method can provide superior results without much time consumption.

4. ULTRASONIC IMAGING FOR REAL CONCRETE STRUCTURE

A series of ultrasonic imaging tests on real concrete structure were conducted to further research on the performance of DMAS method. Firstly, a real reinforced concrete containing several cavity defects was prepared, and the MIRA1040 ultrasonic tomography instrument was used to conduct ultrasonic tests and collect ultrasonic data for imaging. Afterwards, the improvement performance of the modified synthetic aperture method on imaging quality was further verified by comparing the imaging results.

4.1 Specimen prepared and test apparatus

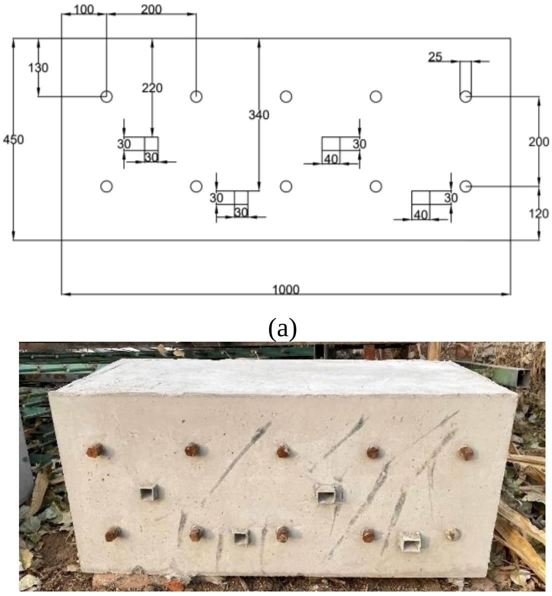

(a)

(b)

Figure 12. Schematic diagram of reinforced concrete specimen with preset defects. (a) Detailed dimensional drawing. (b) Prepared solid model of concrete specimen

To further assess the effectiveness of the DMAS-SAFT and C-DMAS-SAFT methods, an real reinforcement concrete specimen was prepared based on the typical thickness and reinforcement layout of the secondary lining of reinforced concrete in the tunnel, and aluminum alloy square hollow tubes were pre-set to simulate cavity defects. Reinforced concrete specimens were designed to contain void defects of different sizes and depths. The specimens were cast with C40 commercial concrete and compacted with a vibrator. They were demolded after 1 day and cured naturally until 28 days after demolding. The completed model and dimensions are shown in Figure 12. The reinforced concrete specimen measures 1000 mm in length, 600 mm in width, and 450 mm in height. It incorporates internal void defects sized 30 mm and 40 mm, positioned at depths of 260 mm and 370 mm from the surface.

The echo signals were collected using an ultrasonic tomography instrument (A1040 MIRA). The equipment has a 4×12 dry-coupled SH ultrasonic probe array. The main frequency of emitting ultrasonic waves is 50KHz, and the sampling frequency is 1MHZ The equipment uses the method of excitation in the first row - reception in the last 11 rows, then excitation in the second row - reception in the last 10 rows, and so on, to excitation in the 11th row - reception in the last row. Perform data collection in the same manner as in the simulation. Signal processing and post-processing imaging methods were run in MATLAB. The received signals were then imaged using SAFT, DMAS-SAFT and C-DMAS-SAFT respectively.

4.2 Test results and analysis

In order to verify the effectiveness of the improved synthetic aperture imaging method, the imaging effects of 30mm and 40mm defects at deep and shallow positions were analyzed. First, spectral analysis was performed on the imaging data to determine the bandwidth and cutoff frequency of the 2D filter. As in the simulation, it was mainly composed of two frequency components, the DC component and the second harmonic. Once the filter parameters were properly set, band-pass filtering was performed on the image data (***Amp***). After filtering, the second harmonic components were retained, while the DC component and noise were eliminated for image reconstruction (Figure 13).

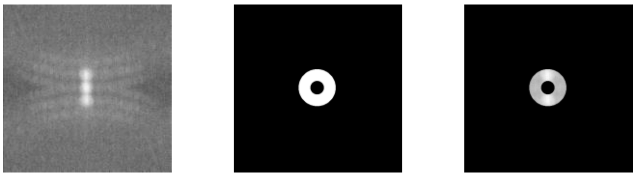

Figure 13. The spectrum of a 40mm length defect at a deep location. (a) The spectrum of the image data before filtering. (b) Represents the spectrum of the filter. (c) Displays the spectrum of the image data after filtering

The ultrasonic imaging results are obtained by SAFT, DMAS-SAFT and C-DMAS-SAFT respectively. It is evident that, compared to traditional SAFT, DMAS-SAFT demonstrated exceptional capabilities in identifying rebars and defects as well as in suppressing noise. In the imaging results for a 40mm defect, the first layer of rebar exhibited strong reflection, showing the highest intensity in imaging energy. Additionally, for shallow internal defects measuring 40mm in length, the traditional SAFT method was capable of effective identification (Figure 14a). However, for a 30mm defect, the reflected energy of the defect in traditional SAFT imaging was very weak so that it is difficult to distinguish the defect, but which can be accurately distinguished in the DMAS-SAFT imaging(Figure 14b). Due to the ultrasonic attenuation, the energy reflected from the second layer of rebar is not strong, resulting in poor imaging of this second layer (Figure 14).

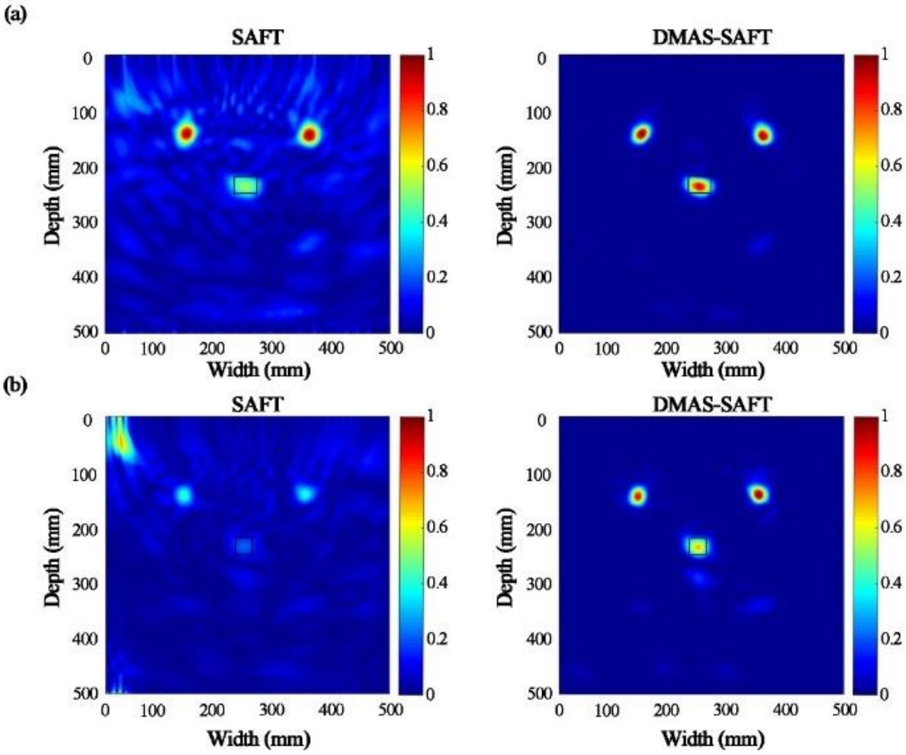

Figure 14. Imaging results of reinforced concrete with defects in a shallow position using three imaging methods. (a) Defect with a length of 40mm, (b) Defect with a length of 30mm. The preset locations of the defects were outlined by a black rectangle

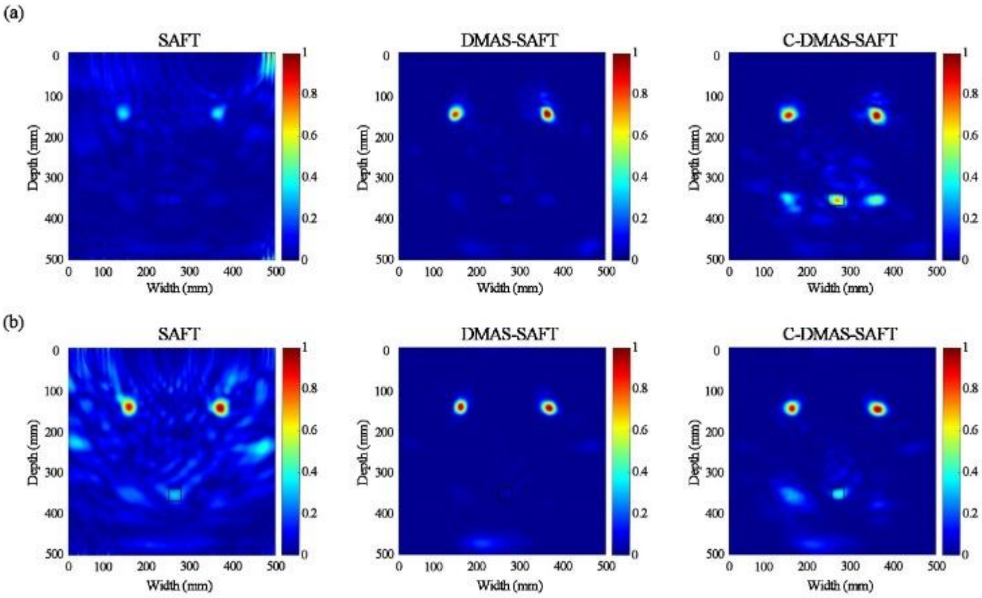

Figure 15. Imaging results of deep defects in reinforced concrete using three imaging methods. (a) represents defect with a length of 40mm, and (b) represents defect with a length of 30mm

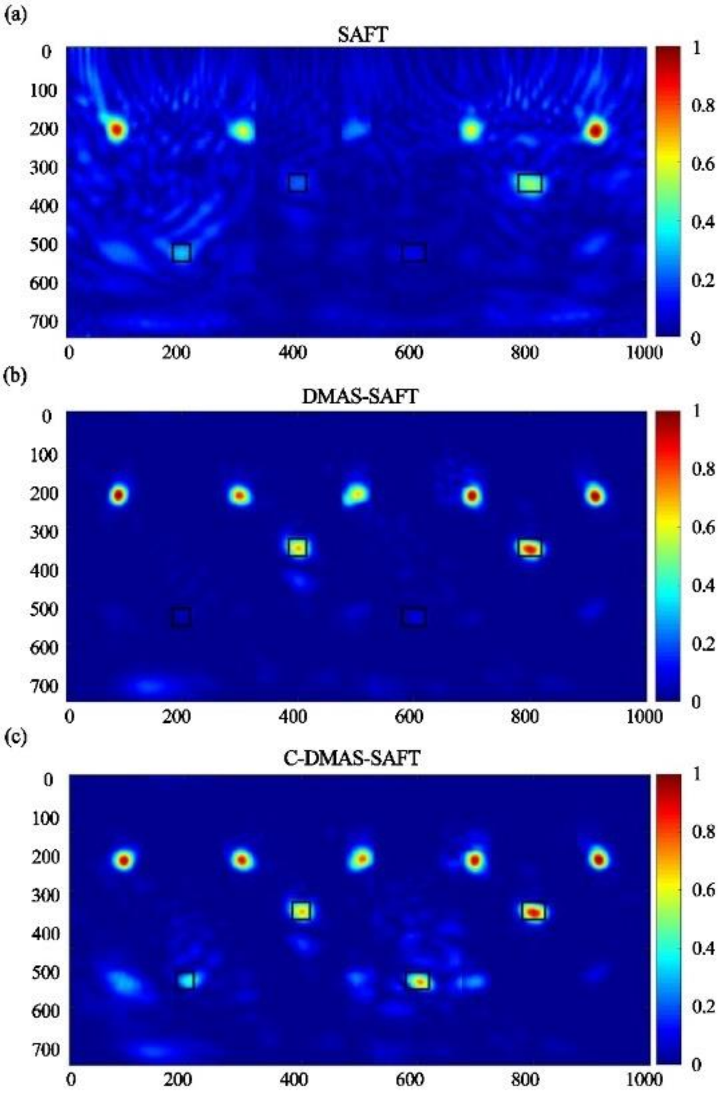

Figure 16. The imaging results of the reinforcement concrete using the three imaging methods. (a) using the traditional SAFT method, (b) using the DMAS-SAFT method, (c) using the C-DMAS-SAFT method

For deep-seated cavity defects in length 40mm and 30mm respectively, the C-DMAS-SAFT method exhibits the best imaging performance compared to both the traditional SAFT and DMAS-SAFT methods. Due to the significant attenuation and absorption of ultrasonic wave propagating in concrete materials, the energy and amplitude of the ultrasonic waves weakens progressively as they propagate through reinforced concrete, which results in the reflected energy of target defects at deep locations being relatively weaker.

Figure15a shows the imaging results for reinforcement concrete region containing a 40mm length defect which located at a deeper position by three methods. According to the imaging results, the traditional SAFT method was capable of detecting the first layer of rebar, but failed to identify the second layer of rebar and the defect, and the surrounding area was plagued with significant amounts of artifacts and noise. Compared to traditional SAFT, the imaging results obtained with the DMAS-SAFT method showed a marked improvement in quality. This method effectively eliminated artifacts and suppressed noise, leading to enhanced imaging. However, it still failed short in detecting defects at deep location. Through increasing the power of the dynamic apodization factor and applying amplitude compensation in line with the ultrasonic attenuation coefficient, it was possible to enhance the energy at deeper layers, thus enabling the detection of deep-seated defects. The results obtained using the C-DMAS-SAFT method demonstrated its ability to identify defects at deeper locations and the second layer of rebar, although it should be noted that this approach also resulted in an increase in background noise.

Figure 15b shows the imaging results for concrete region containing a 30mm length defect which situated in a deeper location by SAFT, DMAS-SAFT and C-DMAS-SAFT respectively. Obviously, the SAFT imaging method was unable to detect the defect due to the image in defect region is very fuzzy. The DMAS-SAFT imaging method successfully detected the first layer of rebars clearly, yet it still failed to identify the defect. However, through increasing the power of the apodization factor to three and compensating the echo signals, the C-DMAS-SAFT method can detect the 30mm defect. Additionally, this adjustment allowed for the rough distinction of the rebars in the second layer.

In order to make the detection image more concrete, the four groups of images obtained were panoramic reconstructed. Firstly, the imaging range was positioned, the overlapping part was taken as the reference point of the steel bar, and the image energy was averaged to obtain the reconstructed image. The reconstructed images of the concrete specimen are shown as Figure 16. According to the reconstructed results, the improved SAFT method significantly suppressed surface noise, and the imaging energy of deep voids and underlying steel bars also increased, visually highlighting the location of voids within the structure, providing a strong guarantee for subsequent defect identification.

In order to quantify the noise suppression capability, the SNR of the image results of different imaging methods was calculated in the same way as in the simulation. The detailed SNR was shown in Table 6. It was observed significant enhancements in SNR for shallow defects when using DMAS-SAFT compared to the traditional SAFT method. For shallow defects measuring 30mm, DMAS-SAFT achieved a substantial SNR improvement of 21.87dB, constituting an increase of 170.73%. For 40mm defect, the SNR enhancement with DMAS-SAFT was 21.67dB, representing a 135.18% increase over SAFT. The average increase in SNR for shallow defects measuring 30mm and 40mm, using DMAS-SAFT compared to traditional SAFT, is approximately 152.95%. In the case of deep defects, the C-DMAS-SAFT method showed exceptional imaging capabilities. For a deep defect of 30mm, the SNR achieved using C-DMAS-TFM was 13.57dB higher than that obtained with traditional SAFT, representing a substantial improvement of 138.89%. Additionally, in the case of a 40mm defect, the SNR observed with C-DMAS-SAFT was 23.87dB. When evaluating deep defects of both 30mm and 40mm, the C-DMAS-SAFT method demonstrates an average SNR improvement of approximately 141.60% over the traditional SAFT, indicating its superior effectiveness in detecting and analyzing deeper defects.

Table 6. The SNR of images based on different methods in experiments

Width	Depth	SAFT	DMAS-SAFT	C-DMAS-SAFT
30mm	340mm	9.77dB	10.41dB	23.34dB
30mm	220mm	12.81dB	34.68dB	
40mm	340mm	5.03dB	11.71dB	23.87dB
40mm	220mm	16.03dB	37.70dB	

The data row located in of middle of the defect imaging region obtained through different imaging methods were used as a lateral projection of defect for comparative analysis, which is shown as Figure 17. According to the figure, the noise of the curves obtained through DMAS-SAFT and C-DMAS-SAFT was almost zero at positions where there is no target, which indicates DMAS-SAFT and C-DMAS-SAFT have strong clutter suppression capabilities. The peak width of the curves obtained from DMAS-SAFT and C-DMAS-SAFT at the defect location was significantly closer to the actual size of the defect. For shallow defects, the energy of images in defect region based on DMAS-SAFT was significantly enhanced compared with SAFT. For deep defects, the imaging energy in defect region obtained from C-DMAS-SAFT was also enhanced, which makes the characteristics of the defects imaging more obvious. Furthermore, the lower amplitude between adjacent peaks clearly distinguished two separate targets, namely defects and reinforcements. A comparison of the error between the actual defect size and imaging peak width at the -20dB level using different imaging methods was presented in Table 7. Among them, the imaging results of both DMAS-SAFT and C-DMAS-SAFT methods have smaller errors than traditional SAFT and are closer to the actual size of defects, which indicates DMAS and C-DMAS-SAFT method can effectively improve the lateral resolution and contrast in ultrasonic imaging.

Table 7. The lateral error between the imaging results and actual defects for the experiments. (unit: mm)

Width	Depth	SAFT	DMAS -SAFT	C-DMAS -SAFT
30mm	220 mm	54.83	32.55	
30 mm	340 mm	49.00	18.80	23.59
40 mm	220 mm	59.56	25.77	
40 mm	340 mm	46.72	22.67	20.78

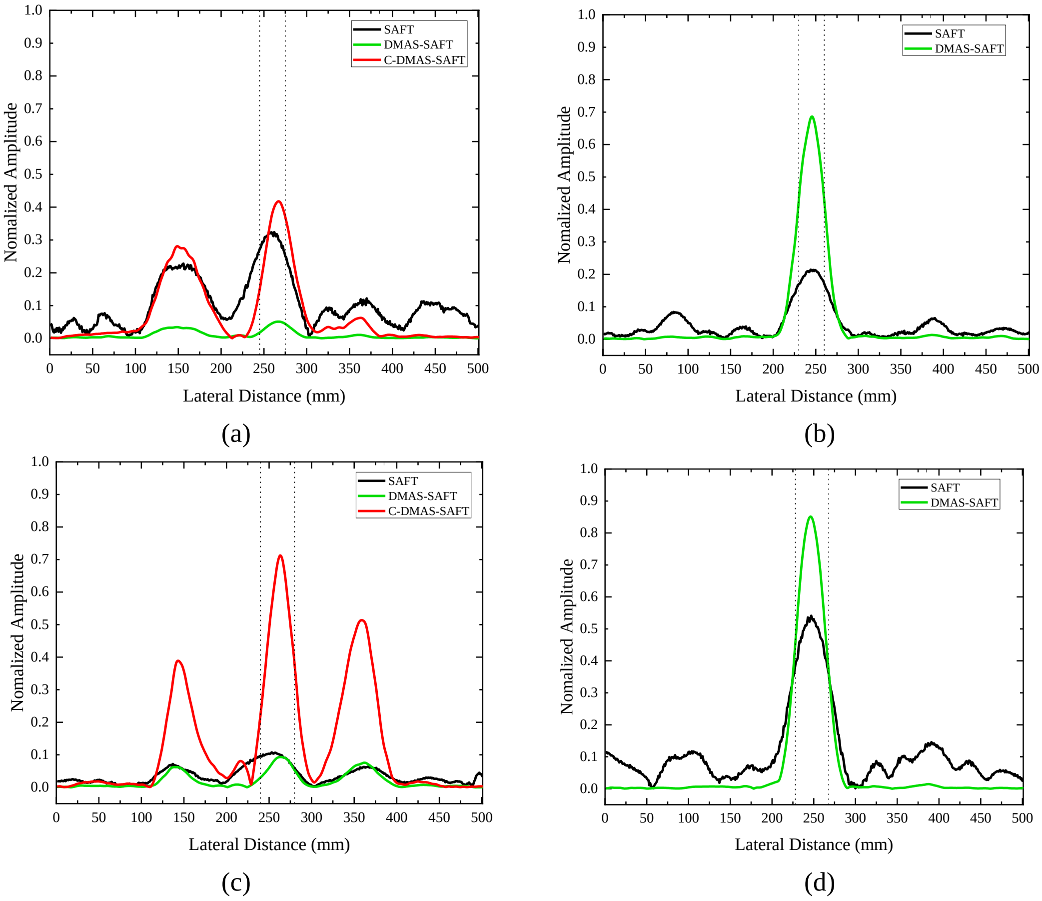

(a) (b) (c) (d)

Figure 17. Comparison of lateral projections of defects in experiments using different imaging methods. (a) 30mm defect, deep location. (b) 30mm defect, shallow location. (c) 40mm defect, deep location. (d) 40mm defect, shallow location

5. CONCLUSION

In the ultrasonic inspection of reinforced concrete structures, the SAFT imaging method often encounters a large number of artifacts and noise, and the ultrasonic waves are severely attenuated inside the structure, causing deep defect features to be submerged, hindering the accurate location of defects. In order to solve this problem, we modified the traditional SFAT method through that replaces the traditional DAS beamformer in SAFT with a DMAS beamformer, which performs a combined coupling, multiplication, and summation process of backscattered echoes to calculate the cross-correlation across the receiving aperture to improve imaging quality, thus proposed two improvement methods DMAS-SAFT and C-DMAS-SAFT. The effectiveness and advancement of these methods were verified through numerical simulation and concrete specimen experiments, and the experiment results show that:

(1) Compared to traditional SAFT, the improved synthetic aperture methods have demonstrated a significant improvement in the SNR. In simulations, the SNR for shallow defects treated with DMAS-SAFT saw an average increase of 92.78%, whereas the SNR for deep defects treated with C-DMAS-SAFT improved by an average of 143.23%. In experimental settings, the average SNR improvement for shallow defects using DMAS-SAFT was 152.95%. Similarly, for deep defects, C-DMAS-SAFT showed an average improvement of 141.60% over traditional SAFT.

(2) The methods we proposed effectively improve the lateral resolution, suppress side lobes, and make the -20dB defect projection closer to the actual size of the defect. In addition, the method enhances the energy targeted at deep defects within concrete structures, thereby improving detection accuracy.

(3) The methods improve imaging accuracy without significantly increasing processing time, offering high computational efficiency, compared with traditional SAFT imaging method. The processing time of SAFT is 1.559s, DMAS-SAFT is 1.639s, and C-DMAS-SAFT is 1.78s.

ACKNOWLEDGMENT

The research was funded by National Key Research and Development Program of China (Grant No.: 2021 YFB2601000), the National Natural Science Foundation of China (Grant No.: U2034207), the Science and Technology Project of Hebei Education Department (Grant No.: QN2020411) and the Scientific and Technological Research Foundation for the Selected Returned Overseas Chinese Scholars (Grant No.: C20210304).

REFERENCES

[1] Han, W., Jiang, Y., Li, N., Koga, D., Sakaguchi, O., Chen, H. (2021). Safety evaluation and failure behavior of degraded tunnel structure with compound diseases of voids and lining defects. Arabian Journal of Geosciences, 14: 1-10. https://doi.org/10.1007/s12517-021-07489-2

[2] Wang, B. (2022). Application of non-destructive testing technology in concrete inspection. Building Technology Development, 49(6): 70-72.

[3] Zheng, Y., Wang, S., Zhang, P., Xu, T., Zhuo, J. (2022). Application of nondestructive testing technology in quality evaluation of plain concrete and RC structures in bridge engineering: A review. Buildings, 12(6): 843. https://doi.org/10.3390/buildings12060843

[4] Cotič, P., Kolarič, D., Bosiljkov, V.B., Bosiljkov, V., Jagličić, Z. (2015). Determination of the applicability and limits of void and delamination detection in concrete structures using infrared thermography. Ndt & E International, 74: 87-93. https://doi.org/10.1016/j.ndteint.2015.05.003

[5] Stryk, J., Matula, R., Pospíšil, K., Dérobert, X., Simonin, J.M., Alani, A.M. (2017). Comparative measurements of ground penetrating radars used for road and bridge diagnostics in the Czech Republic and France. Construction and Building Materials, 154: 1199-1206. https://doi.org/10.1016/j.conbuildmat.2017.06.134

[6] Zhang, L., Dang, F., Ding, W., Zhu, L. (2020). Quantitative study of meso-damage process on concrete by CT technology and improved differential box counting method. Measurement, 160: 107832. https://doi.org/10.1016/j.measurement.2020.107832

[7] Wu, Y., Zhang, J., Gao, C., Xu, J. (2023). Internal defect detection quantification and three-dimensional localization based on impact echo and classification learning model. Measurement, 218: 113153. https://doi.org/10.1016/j.measurement.2023.113153

[8] Tseng, C.W., Chang, Y.F., Wang, C.Y. (2018). Total focusing method or phased array technique: Which detection technique is better for the ultrasonic nondestructive testing of concrete? Journal of Materials in Civil Engineering, 30(1): 04017256. https://doi.org/10.1061/(ASCE)MT.1943-5533.0002118

[9] Wang, G., Chen, Y., Li, Q., Lu, C., Chen, G., Huang, L. (2019). Ultrasonic computerized tomography imaging method with combinatorial optimization algorithm for concrete pile foundation. IEEE Access, 7: 132395-132405. https://doi.org/10.1109/ACCESS.2019.2940766

[10] Kwon, H., Joh, C., Chin, W.J. (2021). 3D internal visualization of concrete structure using multifaceted data for ultrasonic array pulse-echo tomography. Sensors, 21(19): 6681. https://doi.org/10.3390/s21196681

[11] Sanderson, T., Freeseman, K., Liu, Z. (2022). Concrete bridge deck overlay assessment using ultrasonic tomography. Case Studies in Construction Materials, 16: e00878. https://doi.org/10.1016/j.cscm.2022.e00878

[12] Aldo, O., Samokrutov, A.A., Samokrutov, P.A. (2013). Assessment of concrete structures using the Mira and Eyecon ultrasonic shear wave devices and the SAFT-C image reconstruction technique. Construction and Building Materials, 38: 1276-1291. https://doi.org/10.1016/j.conbuildmat.2011.06.002

[13] Hoegh, K., Khazanovich, L., Maser, K., Tran, N. (2012). Evaluation of ultrasonic technique for detecting delamination in asphalt pavements. Transportation Research Record, 2306(1): 105-110. https://doi.org/10.3141/2306-12

[14] Lin, S., Shams, S., Choi, H., Meng, D., Azari, H. (2020). Estimation of wave velocity for ultrasonic imaging of concrete structures based on dispersion analysis. Journal of Testing and Evaluation, 48(2): 1095-1107. https://doi.org/10.1520/JTE20180343

[15] Wu, Y., Wang, Y., Li, D., Zhang, J. (2023). Two-step detection of concrete internal condition using array ultrasound and deep learning. NDT & E International, 139: 102945. https://doi.org/10.1016/j.ndteint.2023.102945

[16] Holmes, C., Drinkwater, B.W., Wilcox, P.D. (2005). Post-processing of the full matrix of ultrasonic transmit–receive array data for non-destructive evaluation. NDT & E International, 38(8): 701-711. https://doi.org/10.1016/j.ndteint.2005.04.002

[17] Zhang, J., Drinkwater, B.W., Wilcox, P.D. (2011). Effects of array transducer inconsistencies on total focusing method imaging performance. NDT & E International, 44(4): 361-368. https://doi.org/10.1016/j.ndteint.2011.03.001

[18] Xiao, H., Shen, Y., Xiao, L., Qu, W., Lu, Y. (2018). Damage detection in composite structures with high-damping materials using time reversal method. Nondestructive Testing and Evaluation, 33(3): 329-345. https://doi.org/10.1080/10589759.2018.1476512

[19] Mustapha, S., Lu, Y., Li, J., Ye, L. (2014). Damage detection in rebar-reinforced concrete beams based on time reversal of guided waves. Structural Health Monitoring, 13(4): 347-358. https://doi.org/10.1177/1475921714521268

[20] Chen, Y., Kong, Q.R., Lu, C., Shi, W.Z., Li, Q.F. (2021). Circular statistics vector weighting for ultrasound coherent plane wave compounding. Chinese Joumal of Scientific Instrument, 42(10): 264-273.

[21] Ge, L., Li,Q., Wang, Z., Li, Q., Lu, C., Dong, D., Wang, H. (2023). High-resolution ultrasonic imaging technology for the damage of concrete structures based on total focusing method. Computers and Electrical Engineering, 105: 108526. https://doi.org/10.1016/j.compeleceng.2022.108526

[22] Guo, X., Han, Y., Nie, P. (2021). Ultrasound imaging algorithm: half-matrix focusing method based on reciprocity. Mathematical Problems in Engineering, 2021: 8888469. https://doi.org/10.1155/2021/8888469

[23] Lim, H.B., Nhung, N.T.T., Li, E.P., Thang, N.D. (2008). Confocal microwave imaging for breast cancer detection: Delay-multiply-and-sum image reconstruction algorithm. IEEE Transactions on Biomedical Engineering, 55(6): 1697-1704. https://doi.org/10.1109/TBME.2008.919716

[24] Matrone, G., Ramalli, A. (2018). Spatial coherence of backscattered signals in multi-line transmit ultrasound imaging and its effect on short-lag filtered-delay multiply and sum beamforming. Applied Sciences, 8(4): 486. https://doi.org/10.3390/app8040486

[25] Matrone, G., Ramalli, A., Tortoli, P., Magenes, G. (2018). Experimental evaluation of ultrasound higher-order harmonic imaging with Filtered-Delay Multiply And Sum (F-DMAS) non-linear beamforming. Ultrasonics, 86: 59-68. https://doi.org/10.1016/j.ultras.2018.01.002

[26] Alshaya, A., Harput, S., Moubark, A.M., Cowell, D.M., McLaughlan, J., Freear, S. (2016). Spatial resolution and contrast enhancement in photoacoustic imaging with filter delay multiply and sum beamforming technique. In 2016 IEEE International Ultrasonics Symposium (IUS), Tours, France, pp. 1-4. https://doi.org/10.1109/ULTSYM.2016.7728682

[27] Jeon, S., Park, E.Y., Choi, W., Managuli, R., Lee, K.J.,

Kim, C. (2019). Real-time delay-multiply-and-sum beamforming with coherence factor for in vivo clinical photoacoustic imaging of humans. Photoacoustics, 15: 100136. https://doi.org/10.1016/j.pacs.2019.100136

[28] Teng, D., Liu, L., Xiang, Y., Xuan, F.Z. (2023). An optimized total focusing method based on delay-multiply-and-sum for nondestructive testing. Ultrasonics, 128: 106881. https://doi.org/10.1016/j.ultras.2022.106881